ORIGINAL ARTICLE

Damping property of a NiTi auxetic structure fabricated through selective laser melting

Adelaide Nespoli[1] · Antonio Mattia Grande[2] · Francesca Passaretti[1] · Daniela Rigamonti[2] · Giuseppe Sala[2] · Paolo Bettini[2]

Abstract
The present work aims at studying the damping response of a NiTi auxetic structure fabricated through additive manufacturing. Furthermore, an electropolishing route has been accounted for improving the roughness on the external surface of the printed samples. The damping capacity of the manufactured auxetic NiTi components is evaluated through the amount of energy dissipated per cycle and through the loss factor index. Results show that the damping capacity of the auxetic NiTi cell takes advantage of electropolishing and it is superior to that of traditional materials. Particularly, a maximum dissipated energy of 55 mJ was registered in the austenite state after 10 min of electropolishing; additionally, the loss factor shows a maximum of 0.0523 in the R-phase.

Keywords Damping · Auxetic · NiTi · Selective laser melting · Additive manufacturing

1 Introduction

NiTi alloys are near-equiatomic intermetallic compounds highly valued for their peculiar behaviors such as shape memory and superelastic effects (SME and SE), as well as for high damping and fatigue properties and high strength and corrosion resistance [1, 2]. The unique combination of physical, chemical, and mechanical properties positions NiTi alloys as candidate structural materials relevant for engineering applications such as aerospace [3].

A diffusionless thermoelastic martensitic transformation (TMT) between two solid phases, austenite and martensite, is the basic principle of the superior mechanical properties of NiTi. Austenite is the parent phase, which is stable at high temperatures and presents a body-centered cubic structure (B2). Martensite is a softer phase that is stable at low temperatures and can be present in multiple variants (twinned martensite) due to its low symmetry (B19'). An additional martensite phase with trigonal structure, called the R-phase, may also appear, generating a two-step transformation. TMT is characterized by thermal and mechanical hysteresis and growth and shrinking of martensite upon cooling and heating [4]. The kind of effect that can occur as a result of the TMT (whether it is SME or SE) is governed by the characteristic transformation temperatures of the alloys, namely by the start and finish temperatures respectively of martensite (Ms and Mf) and austenite (As and Af). The transformation temperatures of NiTi strongly depend on the microstructure; factors such as nickel content, heat treatments, or additional elements, both alloying elements and impurities, are important for controlling the material's thermo-mechanical behavior [4–6].

SME occurs when a specimen, deformed at a temperature below Mf (that is in the martensite phase), regains its original undeformed shape when heated to a temperature above Af (that is in the austenite phase). The motion produced through the change of phase is exploited to produce mechanical work; thus, it finds numerous applications in the actuation field. On the other end, the SE occurs in the austenite state when an external stress induces a martensitic transition and leads to a strain. Upon loading, the austenite first behaves like a common elastic material. Thereafter, when a critical

✉ Paolo Bettini
paolo.bettini@polimi.it

1 Consiglio Nazionale delle Ricerche—Istituto di Chimica della Materia Condensata e di Tecnologie per l'Energia (CNR-ICMATE), Via G. Previati 1/E, Lecco 23900, Italy

2 Politecnico di Milano—Dipartimento di Scienze e Tecnologie Aerospaziali (DAER), Via La Masa 34, Milano 20156, Italy

stress is reached, austenite transforms into a stress-induced martensite (SIM). The transition into SIM happens at an almost constant load thanks to the high mobility of the interfaces of the martensite variants, which minimizes the strain energy allowing high deformation at almost constant stress. Once martensite is completely detwinned, the common linear elastic behavior of the martensite occurs. At austenite temperature, SIM is thermodynamically unstable. Therefore, when the load is removed, the material returns to the austenitic parent phase. Apparent plastic strain of the stress vs. strain curves is therefore recovered, showing a closed loop in the curve. This means that SE is a reversible, not linear, elastic phenomenon [4]. The superelastic characteristic curves can have both a "flag" shape, typical of specimens with strong texture such as wires, or a "leaf" aspect, common for more complex geometries. In both cases, thermo-mechanical hysteresis can be very attractive in practical applications to dissipate mechanical energy and prevent or reduce structural damage due to vibrations.

A superior damping response can be achieved by shaping the NiTi pseudoelastic element in a particular geometry such as that of auxetic structures.

The auxetic geometries are of interest primarily for their enhanced mechanical properties such as high stiffness and high energy dissipation capacities [7–9], as well as for lightweight and low relative density [10], thus they are emerging solutions for many engineering applications such as aerospace [11]. Auxetic geometries, also known as re-entrant structures, show a unique behavior such that their Poisson's ratio is negative. It means that when these solids are compressed, they become smaller in the cross-section direction, or they respond with a complex flexure behavior [12–15]. Moreover, they are usually cellular structures, solids formed by an interconnected network of arms or plates forming edges or faces of a single cell that is spatially repeated [16]. Existing and potential applications of auxetic structures span from aerospace and automotive to the biomedical, military, textile industry until as reinforcement fibers in composites, and as sensors and actuators in smart structures [17].

Therefore, the realization of auxetic structures showing PE property of NiTi seems to be very attractive for damping applications. However, only quite simple geometries are obtained by traditional manufacturing processes due to the very low machinability of NiTi material [18]. Nevertheless, nowadays, the use of NiTi in simple forms such as wires, stents, or ribbons is well established. The main uses of NiTi are medicine (such as stents, grafts, orthopedic staples, orthodontic archwires, and eyeglass frames), aerospace and military (such as couplers in F14 planes), safety (like dampers of seismic vibrations and sprinklers), and robotics (such as actuators) [19–28]. With the advent of the additive manufacturing techniques, the study of these alloys took a further alternative path in the fabrication of complex geometries with superior mechanical properties for the exploitation of the material peculiar characteristics.

Among the various additive manufacturing technologies, selective laser melting (SLM) is one of the most employed and effective techniques for metals [29–34]. It uses a laser beam to selectively melt a bed of metal powder layer after layer, following a CAD (computer-aided design) model. SLM enables the fabrication of near-fully dense three-dimensional objects with peculiar characteristics: homogenous composition equivalent to that of the feedstock, directional oriented parts that present a microstructure characterized by columnar grains extending over multiple layers, and a homogeneous material microstructure with low impurity pick-up. The process parameters and their proper selection are the most powerful tools to guarantee the final high quality of the products through SLM. Therefore, their optimization is of primary importance to achieve both high-density levels of the parts and low impurity pickup. There exist several kinds of parameters that can be divided into four main families depending on their relation to energy (laser power and spot size), environment (power bed and power feed temperature and their uniformity, oxygen content), scan (scan speed, spacing, pattern, strategy), and powder (particle shape, size, distribution, bed density, and layer thickness). The energy density, E, has been used by many authors as the key value that gives a straightforward idea of the overall process. It is defined as the ratio between the laser power, P, and the product between the scan speed, the hatch distance, and the layer thickness [35].

In recent years, many efforts on the printability of NiTi through SLM have been made. There are several interesting papers on the printability of NiTi, such as [36–38]. By now, the production of complex NiTi components is mainly limited to small parts. Xiong et al. [39] fabricated a lath-shape starting from NiTi powder with 50.4 at. % of Ni. With a laser power of 120 W, a scan speed of 500 mm/s, a layer thickness of 30 μm, and a hatch distance of 80 μm, they obtained specimens that exhibit tensile strain of 15.6%. Li et al. fabricated a NiTi (55.7 wt.% Ti) auxetic component of $26 \times 26 \times 36$ mm^3, with nominal arm thickness of 0.3 mm [40]. However, the authors report that the actual arm thickness is much larger due to powder lumps attached to the surface of the components. Problems related to geometrical variation between CAD files and manufactured parts are common. Saghaian et al. [41] realized triply periodic minimal surfaces with a measured porosity 10% higher than the nominal value. They realized $9 \times 9 \times 9$ mm3 NiTi parts (50.1 at. % Ni) with laser power, scanning speed, layer thickness, and hatch spacing of 250 W, 1250 mm/s, and 30 and 120 μm, respectively. Saedi et al. [42] reported that the irreversible strain tends to increase as the porosity level increases, i.e., the thickness of the arms becomes thinner. Indeed, as the thickness of the arms decreases, the local stresses increase at

the same nominal applied stress levels, and so both martensite transformation and plasticization trigger earlier. Other works on lattice NiTi components realized through selective laser melting are reported in the works of Ravari [43].

Based on a previous study [44], this work is aimed at finding a new way to improve the damping response of NiTi components fabricated through SLM. Particularly, the combination of energy dissipation capabilities of an auxetic geometry with the superelastic characteristic properties of NiTi was assessed for the first time. Specimens went first through a two-step thermal route to improve the mechanical response and to a. surface finish through electropolishing to avoid both crack generation as well as a reduction of the fatigue resistance [45]. Damping capability of the printed NiTi specimens was assessed through loading–unloading mechanical tests and through the evaluation of the loss factor index [46]. Finally, a study on local strains on ABS auxetic samples was performed to evaluate the effective auxetic response decoupled from the pseudoelastic one.

2 Materials and methods

Micrometric spherical NiTi powder with 55.2 wt.% of Ni and size ranging between 15 and 45 μm (D50 approximately 30 μm) was purchased from TSL Spezialpulver gmbh (Germany). The feedstock was the same as the one used in [44]. Auxetic samples were fabricated through a selective laser melting machine (AM400, Renishaw) equipped with

a 400 W Ytterbium fiber laser. The manufacturing process is run at room temperature in a reduced building volume (RBV) on a NiTi plate of 78×78 mm^2 surface and 55 mm high. During the process, the building chamber is maintained in a controlled argon atmosphere with oxygen content lower than 500 ppm. Process parameters were selected to produce nearly fully dense parts with good damping properties [35, 44]. According to previous studies, the laser power, the scan speed, the hatch distance, and the layer thickness were respectively kept to 250 W, 1000 mm/s, and 100 and 30 μm.

In this work, the "A"-shaped auxetic structure was selected [10]. It is composed of the 3D repetition of a single unit cell to create a spatially distributed solid geometry. As far as regards the unit cell, differently from the literature reference, the thickness, T, of the structure is maintained constant in this work. The characteristic dimensions are the length of the long inclined structs, M, the length of the short inclined struct, N, and the height of the cell, H, see Fig. 1(a). Moreover, the angles between the horizontal direction and the axis of both the long and short structs are defined

Table 1 Auxetic geometry characteristic lengths and angles

M [mm]	3.54
N [mm]	1.50
H [mm]	2.06
T [mm]	0.5
φ [°]	65
θ [°]	50

Fig. 1 2D CAD model of the unit cell and of the auxetic structure (**a, b**); 3D representation of the auxetic element (**c**). Unit of the 2D CAD model: mm
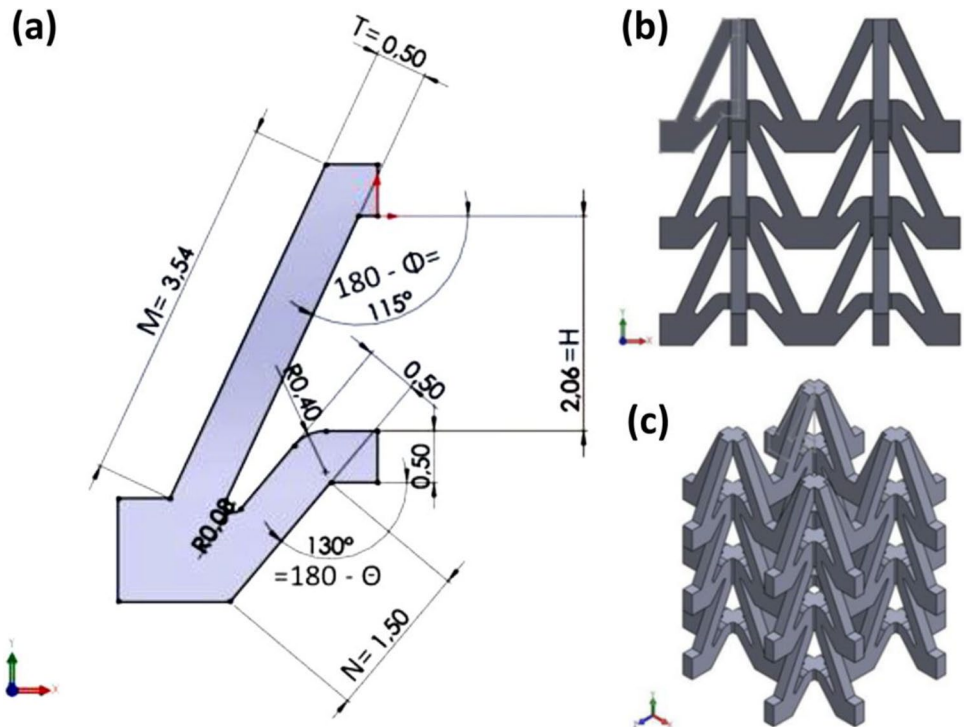
as φ and θ, respectively. Table 1 lists the characteristic dimensions selected for the auxetic element. The choice of dimensions is mainly driven by the SLM fabrication constraints and limitations. The thickness is fixed at 0.5 mm, being near the minimum thickness of complex geometry parts that can be fabricated with the SLM machine. Another constraint is imposed by the process on the angles: to avoid the use of supports, they must be larger than 45° with respect to the horizontal direction; thus, to take margins during the building process of the NiTi part fabrication, φ has been defined equal to 65° and θ to 50°. The auxetic geometry was designed to be tested in compression; consequently, a square base of approximately 10×10 mm^2 was chosen to assure a stable base during tests, and the overall height was fixed to approximately 10 mm to avoid buckling issues. Thus, the global geometry results in four "A" shaped columns composed of three rows of unit cells, shown in Fig. 1(b) and (c). Furthermore, the base has been set as a square of about 10 mm of side maximum length to avoid excessive internal stresses due to heat during the fabrication process that may detach the component from the building plate. The fillets have been added to avoid extreme stress concentrations in the parts.

The auxetic functioning was first checked by observing the position of some characteristic points during a quasi-static compression test, see Fig. 2. In Fig. 2, L_{TOT} is the total high; L_1, L_2, and L_3 represent the distance between a reference point (situated on the testing grip) and representative points of the sample (A_1, A_2, B_1, B_2, C_1, and C_2), each situated on the three-unit rows; w_1 and w_2 symbolize two characteristic horizontal widths. Mean values were calculated over three measurements. The characteristic points were observed in two frames of a video taken during a compression failure test. The two frames, namely, frames 1 and 2, respectively, represent the auxetic element at the beginning of the compression

test and shortly before failure. Additionally, auxeticity of the printed elements was verified through the calculation of the Poisson ratio. The Poisson ratio was evaluated by Eq. 1 based on the obtained data:

$$\upsilon = -\frac{\epsilon_{\text{lateral}}}{\epsilon_{\text{axial}}} \tag{1}$$

where $\epsilon_{\text{lateral}}$ is the relative lateral strain of the sample calculated as $\frac{\Delta w}{w_0}$ (w_0 is the sample width, 9.41 mm) and ϵ_{axial} is the relative longitudinal (axial) strain of the sample calculated as $\frac{\Delta L}{L_0}$ (L_0 is the sample length, 10.31 mm).

The auxetic geometry was further analyzed to map the strain distribution in the arms (short and long structs) and to understand the actual load condition decoupled from the pseudoelastic effect. To this end, enlarged auxetic samples were prepared (considering a scale factor of 5 with respect to the NiTi original one). These structures were made of ABS + (acrylonitrile butadiene styrene plus) by 3D printing through a Stratasys Dimension Elite printer. While maintaining the proportionality of the deformation field, both the enlargement and the use of a polymeric material allow amplifying strains, facilitating their measurement. Local strains were measured through fiber optic (FO) sensors during compression tests. By exploiting the properties of the guided light, it is possible to create various FO sensors using different principles. In this work, FBG (fiber Bragg grating) sensors were chosen to obtain an average measurement over a short segment (3 mm). The advantages over a more traditional strain gauge reside in the extremely small size of the FO (0.195 mm), which allows good accuracy even without a larger surface for installation, and in the multiplexing, which reduces the cabling needed even with more measuring points. In this analysis, three FBG sensors were respectively bonded on two long and one short arms, Fig. 3. Micron optics
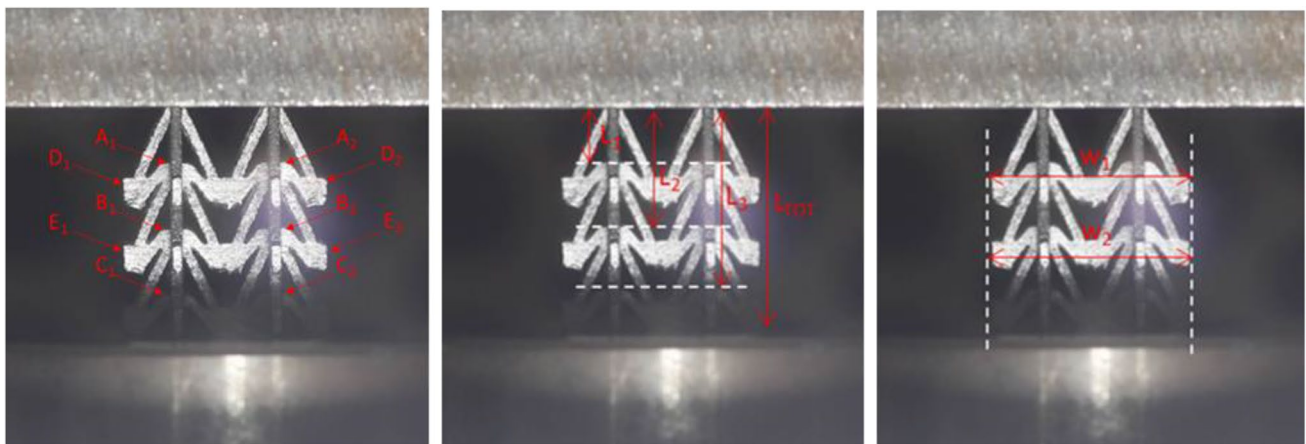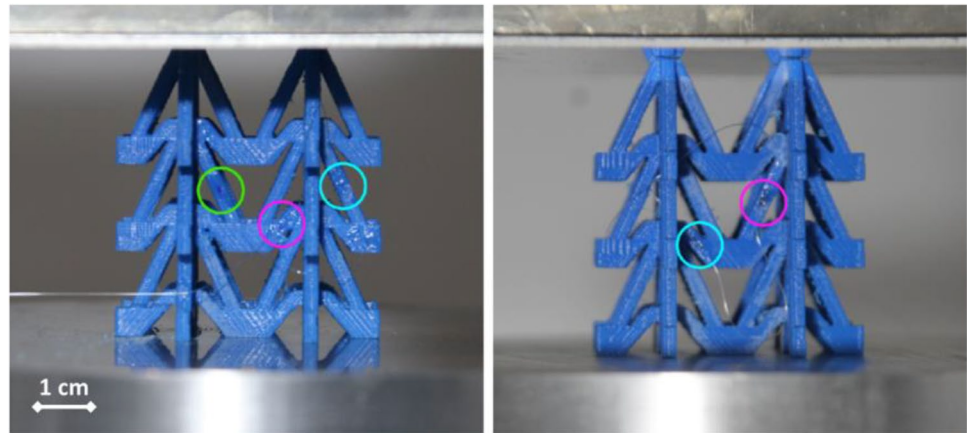

Fig. 2 Characteristic points and variables used to check the auxetic functioning

Fig. 3 ABS auxetic specimens. Circles highlight the position where optical sensors were bonded

instrumentation was used to acquire the signals of the FO sensors.

Regarding the mechanical characterization of the NiTi printed parts, the as-built specimens followed a thermal treatment consisting of a solution annealing at 950 °C for 6 h and aging at 350 °C for 2 h, both followed by water quench at room temperature.

After aging, the samples were electropolished to remove unmelted powder and surface defects. Electropolishing was accomplished at 0 °C in a solution of 90% 2-butoxyethanol and 10% perchloric acid. The electrical tension between cathode (placed inside the medium) and anode (i.e., the sample) was set to 40 V. Immersion time was 12 min, composed of six steps of 2 min each. At the end of each electropolishing step, the sample was cleaned with alcohol and dried with hot air. Thereafter, it was analyzed through a scanning electron microscope (SEM TM3000) to check the size. Measurements were accomplished on twelve arms of the same sample and three measurements were performed on each arm.

The phase transition temperatures of the auxetic parts were assessed through differential scanning calorimetry (Q100 TA Instr.). During thermal analysis, the sample followed a 10 °C/min thermal cycle from -120 to 150 °C. The phase transformation temperatures were identified through the tangent method.

Compression tests on auxetic components were performed with an Instron EP E3000 machine. A single sample for each electropolishing condition was tested. Quasi-static tests were accomplished over two loading–unloading cycles. Tests were conducted at $Af - 10$ °C, Af, and $Af + 10$ °C temperatures and at 3% strain. Furthermore, compression tests till failure were performed on the sample that was electropolished for 8 min. Failure test was accomplished at $Af + 10$ °C, at 2% strain, and at 1 Hz solicitation frequency. Stereomicroscope wild was used to check the sample after the test. Finally, the key factor used to assess the damping behavior of the auxetic structure was the tanδ (namely the

loss factor value), calculated as the ratio between the loss and the stored energy.

3 Results

Figure 4 depicts the auxetic NiTi printed specimens on two building platforms. Figure 4(a) and (b) show the auxetic parts that are supported by thin inclined holders melted to the outermost horizontal segments of the specimens and that were removed after the process. Figure 4(c) shows the auxetic NiTi sample after the thermal treatment route.

Table 2 lists the values of the characteristic variables used to check the auxetic property. Δ is the percentage change of each variable. It can be first noticed that all the variables decrease as the test progresses (negative Δ values). It demonstrates that during compression, the characteristic points A_1, A_2, B_1, B_2, C_1, and C_2 move in the opposite direction to the grip. At the same time, D_1 and E_2 move closer to D_2 and E_2, respectively. This finding confirms qualitatively the auxetic behavior of the "A"-shaped NiTi elements. Considering $L = L_{TOT}$ and w equal to the arithmetic mean between w_1 and w_2, we obtain $\Delta L = -0.23$ mm and $\Delta w = -0.071$ mm. Therefore, by applying Eq. 1, the Poisson ratio of the considered A-shaped structure is -0.344. Henceforth, the calculation of the Poisson ratio validated the auxeticity of the proposed geometry. However, it was observed that the auxetic response is not homogeneous since Δ decreases as the distance from the considered reference point increases (i.e., $L_1 > L_2 > L_3$ and $w_1 > w_2$). The explanation of this anomalous trend is reported in the Discussions section.

To study local strains, three compression cycles were performed on the ABS + auxetic samples, see Fig. 5(a). Apart from an initial nonlinearity of contact common to all the tests performed, the global behavior is mainly linear, even though a noticeable hysteresis probably ascribes to the testing setup. Considering the local strain trend during a
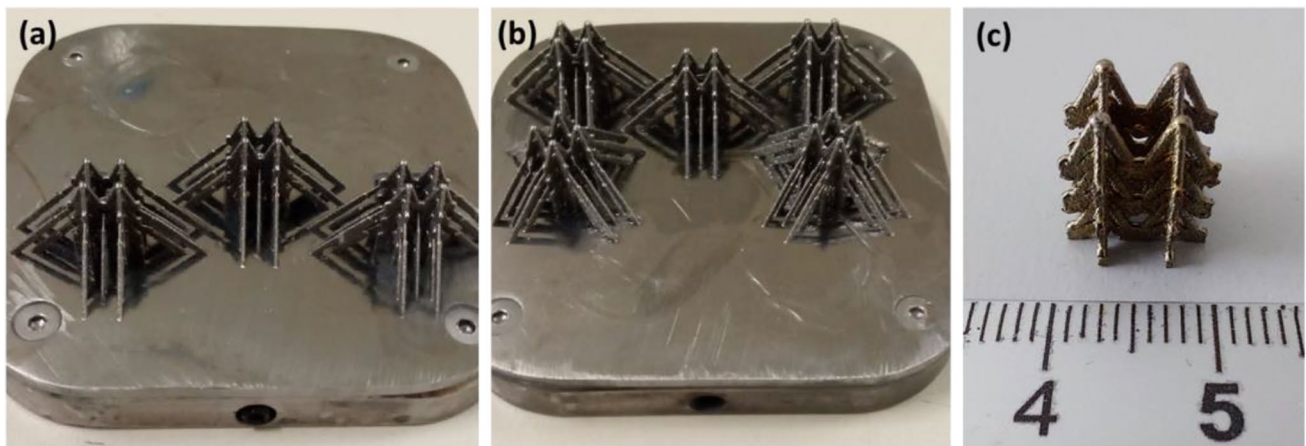
Fig. 4 Photographs of the auxetic NiTi pseudoelastic samples on the building platform (**a**, **b**) and after the thermal treatments (**c**)

Table 2 Characteristic variables taken at two different times of a compression test. Frames 1 and 2 are respectively taken at the beginning of the compression test and just before failure

	Frame 1		Frame 2		
	Mean [mm]	Std. dev	Mean [mm]	Std. dev	Δ [%]
L_{TOT}	20,853	0.191	20,627	0.134	− 1.087
L_1	5293	0.057	5020	0.000	− 5.164
L_2	11,297	0.035	10,960	0.017	− 2.980
L_3	17,207	0.110	16,860	0.046	− 2.015
w_1	18,333	0.064	18,257	0.029	− 0.418
w_2	18,283	0.012	18,217	0.025	− 0.365

single load cycle, Fig. 5(b), it was found that both the two long arms, the inner and the outer, are in tension, whilst the short arm is compressed. Furthermore, a perfectly linear correlation between load and local strain was observed (Fig. 5c).

Figure 6 reports the trend of the mean values of the arm size after the electropolishing steps. It is worth noticing that the size of the as-built specimen (0-min electropolishing) is

higher than the nominal one (approximately 40% higher). Additionally, the as-built sample presents partially molten particles on the surface, see Fig. 7(a). The appearance of the unit cell becomes smothered with the increase of the electropolishing time, see Fig. 7 from (b) to (g). Unmelted particles are no longer visible after 8 min of electropolishing.

The surface finish of the auxetic specimens affects the DSC response. In Fig. 8, it can be observed that the DSC appearance changes with electropolishing time. R-phase peaks (AtoR and RtoA) are most noticeable on the specimen electropolished for 12 min. Furthermore, partially melted particles on the sample surface generate spikes on the RtoM peak (see as-treated condition, 0 min EL curve). Despite these particularities, austenite finish temperature, Af, is approximately 45 °C for all specimens. According to this, mechanical quasi-static tests were accomplished at 35 °C, 45 °C, and 55 °C.

The results of the mechanical tests are visible in Fig. 9. A leaf-shaped mechanical response was observed for all samples. Furthermore, as expected, the load increases with the test temperature for all specimens (Clausius–Clapeyron relationship).
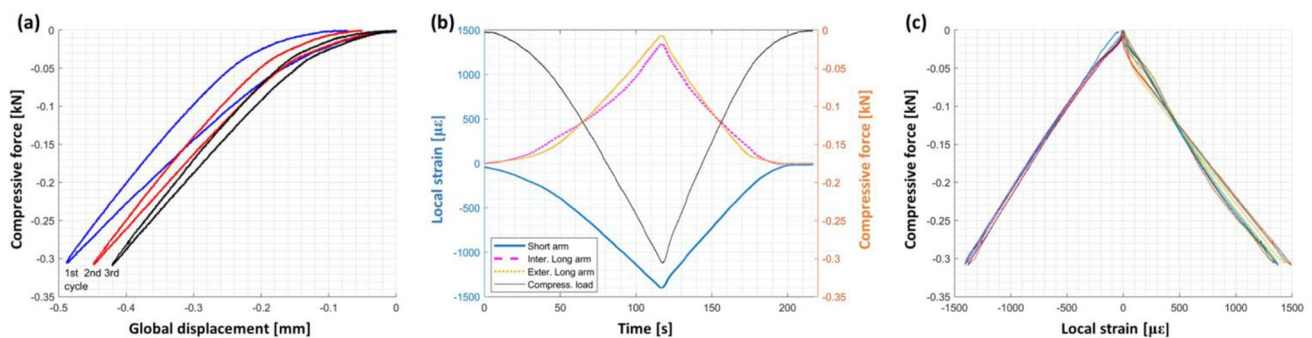

Fig. 5 Analysis of the load and the local strain of the auxetic geometry, with FO measurements. Load cycles (blue: first cycle, red: second cycle, and black: third cycle) (**a**); strain and load trend during test (**b**); load and strain correlation (**c**)
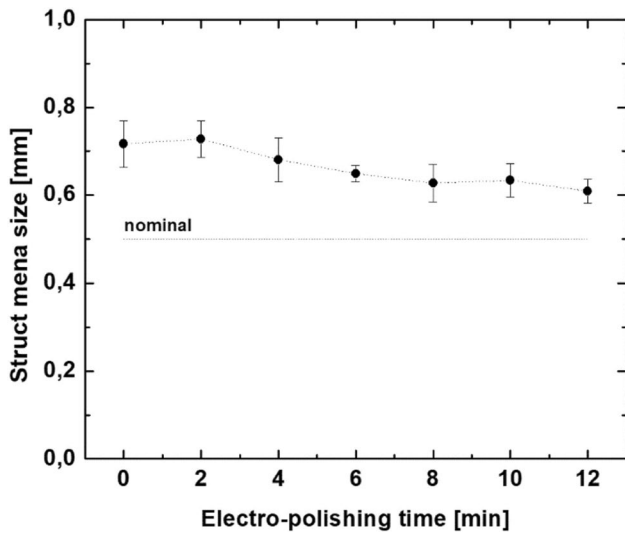
Fig. 6 Arm mean size as a function of the electropolishing time

According to the mechanical data reported in the graphs of Fig. 10, the highest dissipated energy and loss factor were observed for the auxetic sample that followed 10 min of electropolishing. Besides, the reduction of section due to electropolishing was detrimental for the auxetic sample that followed 12 min of electropolishing, which presents the lowest maximum force. Furthermore, it is worth noticing that the loss factor is highest when the material is in an intermediate state, that is, it has not completed the transformation from the R to the austenite phase (i.e., $Af - 10$ °C condition). However, results show that this intermediate state has also the highest residual strains.

Finally, mechanical cycling was studied on sample that presents the lowest residual strains, which is the one that followed the electropolishing route for 8 min. A steep decay of the loss factor was observed during mechanical cycling at 1 Hz, see Fig. 11(a). After 500 mechanical cycles, the loss factor stabilized to approximately 0.01. The sample
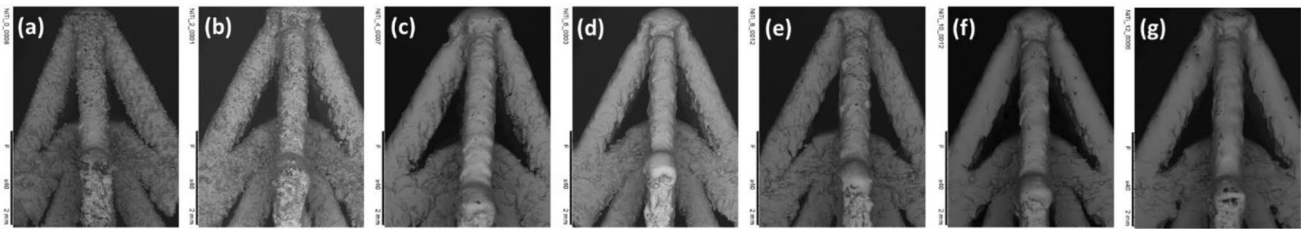

Fig. 7 SEM images of the auxetic structure after the 0 min (**a**), 2 min (**b**), 4 min (**c**), 6 min (**d**), 8 min (**e**), 10 min (**f**), and 12 min (**g**) of electropolishing

Fig. 8 DSC graphs of as treated (0 min EL) and treated + electropolished specimens (time of electropolishing: 8 min, red line, 10 min, purple line, and 12 min, green line)
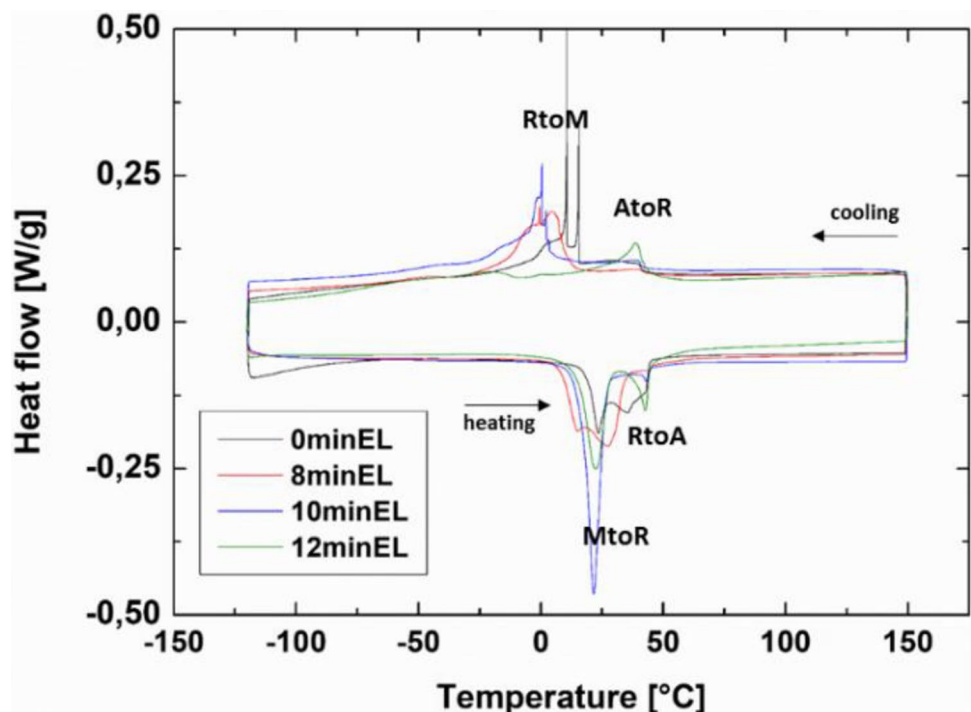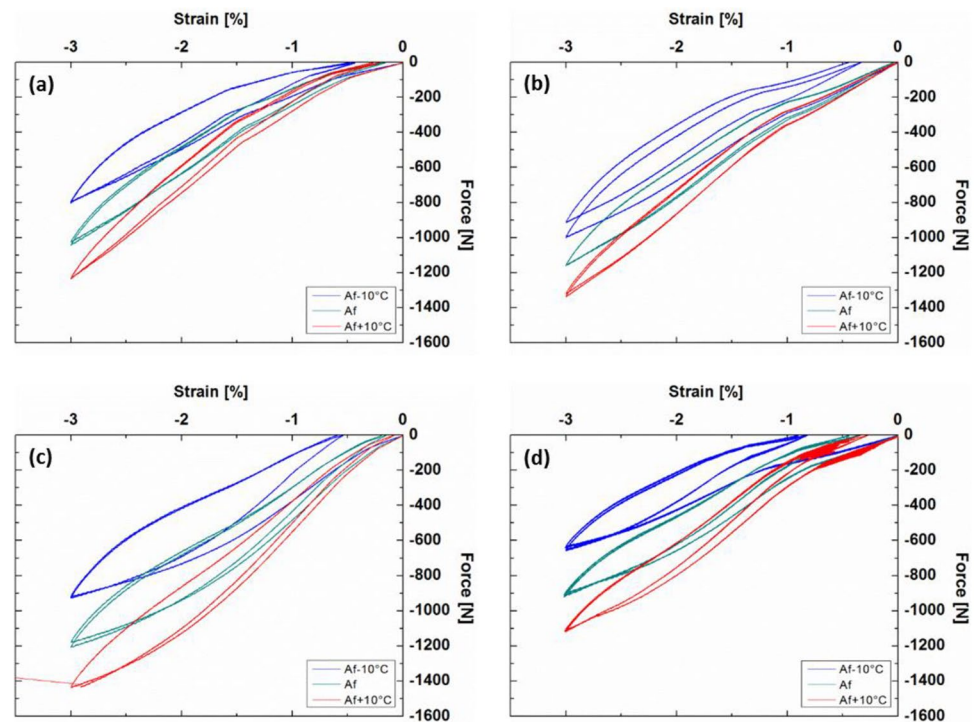
Fig. 9 Quasi-static compression test on not electropolished (**a**) and electropolished (**b** 8 min, **c** 10 min, and **d** 12 min) samples

broke close to cycle number 4000. Optical microscope observations of Fig. 11(b) show that fractures were located on the short arms.

4 Discussions

This work reports on the possibility of fabricating highly performant dampers by exploiting (i) the material superelastic NiTi properties, (ii) the auxetic geometry, and (iii) the additive manufacturing.

The "A"-shaped auxetic NiTi structure was studied. It was found that the fabricated structure behaves like an auxetic material since a negative Poisson ratio was found. However, a not homogeneous response was noticed. This is primarily ascribed to the test set-up, which creates a constraint to the free movement especially of the base of the sample. To enable free movement of the arms during compression, the base of the auxetic sample should be sustained by feet that raise the sample from the testing plate during the compression.

The arms of the as-built samples present a mean size of 0.717 ± 0.053 mm, which is approximately 40% higher than the nominal one (0.5 mm), Fig. 6. The poor geometrical accuracy of the as-built samples is first attributed to the unmelted powder on the sample surface. After the removal of the unmelted and partially melted powder, the size of the arm is 0.628 ± 0.043 mm, which is 25% higher than the nominal one. This is probably ascribed both to the limit of the technology in the fabrication of thin wall structures

and to the process parameters. In particular, the process parameters that should be fine-tuned to obtain CAD-compliant dimensions are the ones that refer to the borders, the up-skin, and the down-skin.

Furthermore, it was found that an electropolishing step is mandatory to avoid a multistep phase transition, which is due to compositional inhomogeneity between the core and the outermost part of the sample after the two-step thermal treatment. It is therefore recommended to remove particles from the samples' surface through the electropolishing route before the thermal treatment to avoid microstructural inhomogeneity in the parts. Furthermore, longer electropolishing inevitably causes the decrease of the maximum force, as observed for the sample that followed 12 min of polishing (Fig. 9). Additionally, electropolishing also enables higher dissipated energy per cycle with respect to the not electropolished condition.

The leaf-shaped mechanical response of the auxetic structure is mainly ascribed to a not-uniform state of stress in the sample. For common pseudoelastic elements, the starting point for the not linear elastic plateau is determined by the transformation of the austenite in the martensite phase, which once transformed, continues detwinning as the load increases, generating the well-known superelastic plateau (stress-induced martensite). Therefore, in the case of wires in tension, where the state of stress is uniform, the starting point of the plateau is neat and the plateau itself is straight. On the other end, when dealing with complex geometry such as auxetic structures, the state of stress is not uniform, and
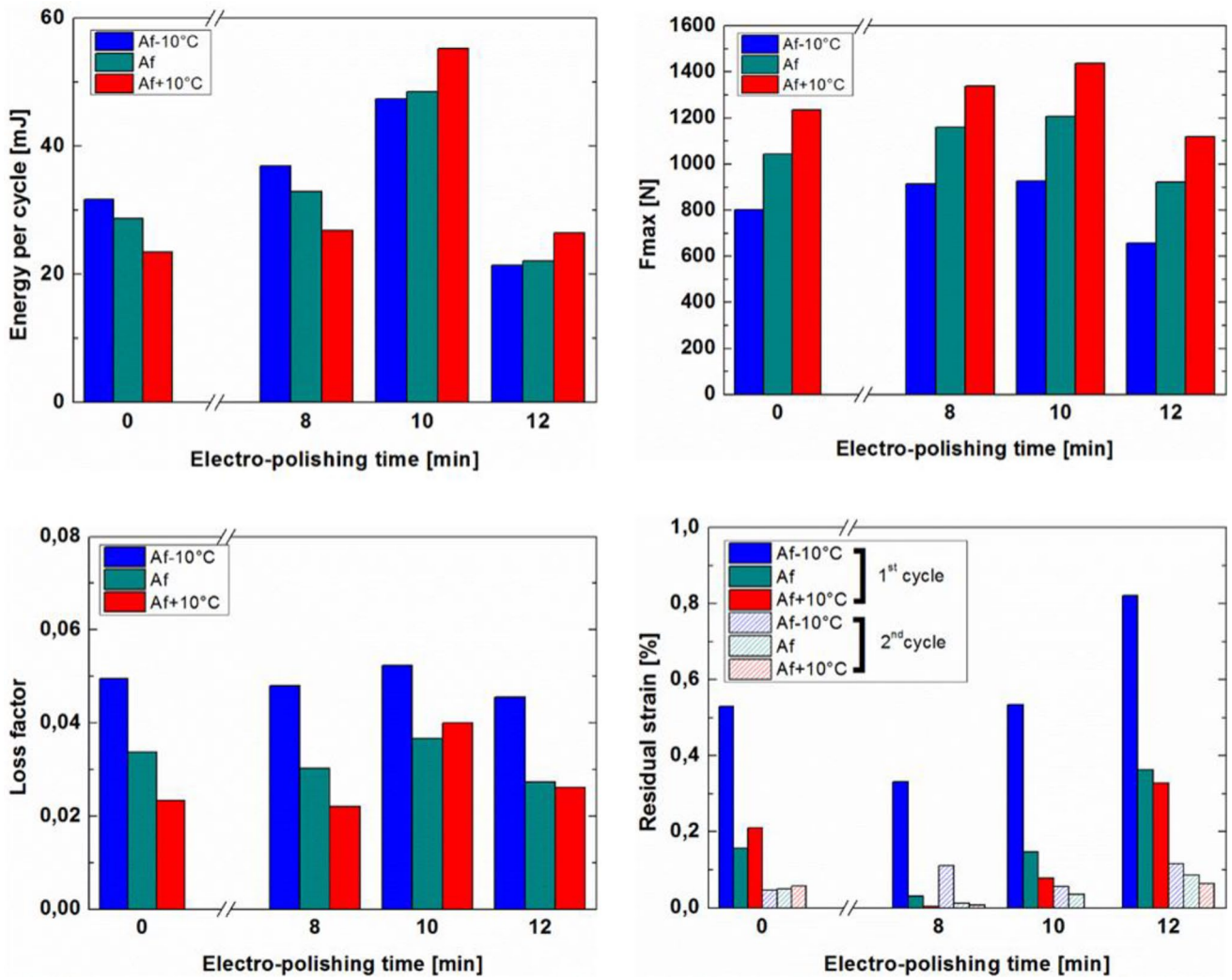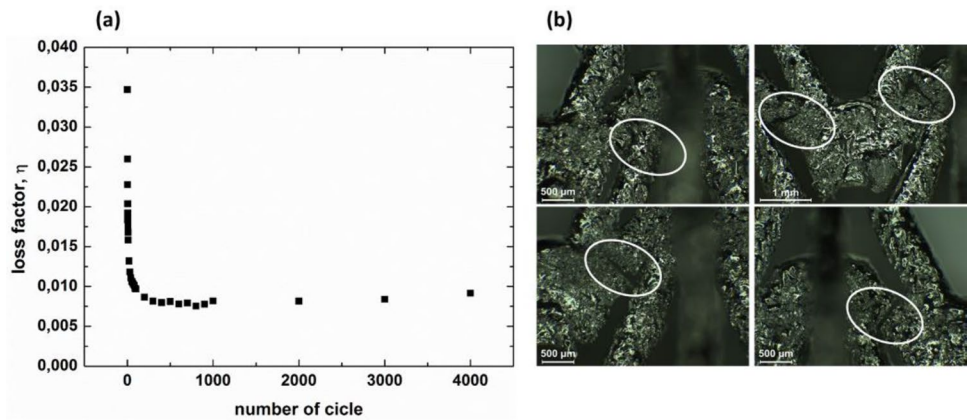
Fig. 10 Dissipated energy, maximum force and loss factor registered at the second mechanical cycle and residual strains registered at the end of the first and at the second mechanical cycle

Fig. 11 Loss factor of the 8-min electropolished sample registered during mechanical test at 55 °C (1 Hz, 2% strain) (**a**). Fracture zones (**b**)

the martensite transforms gradually. While in some areas of the structure, the martensite is detwinning (plateau), others are transforming (starting point) or still in the austenitic phase (linear elastic trend); this leads to a more complex leaf-shaped behavior. The leaf shape gets thinner with the increase in the test temperature. It was observed that at a temperature just below Af (Af − 10 °C condition) the loss factor is higher than that registered at a higher temperature. It means that the damping capacity is enhanced when the material is not completely transformed into the austenite state. However, as a counterpart, at this temperature, the material shows the highest residual strain.

Despite the thin hysteresis, a good damping capacity was registered. Comparing results with those of literature [44], it can be noticed that the loss factor of the auxetic NiTi structures is higher than that of standard materials and comparable with the NiTi bars produced through SLM. The not superior damping response with respect to other NiTi-printed parts is primarily ascribed to the difficulty of making each part of the auxetic structure collaborate in damping. From the point of view of the material, high damping means inducing the transformation (SIM) at every point of the structure. For simple geometries, it is easier to induce this transformation homogeneously in all the material and consequently produce a high damping response. On the other hand, it is not obvious that high damping can be achieved in every part of the auxetic structure. In fact, as complexity increases, it is more difficult to minimize local effects that block the phase transformation. This means that further investigations should be considered in order to understand the stress (strain) distribution in complex structures such as the auxetic ones. One way consists in decoupling the damping response of the material with that of the structure. In the present work, it was observed that the long and short arms have an opposite response; the two structs are respectively tensioned and compressed during a global compression. This result is consistent with the auxetic behavior of the structure, in which the central node descends along the plane of vertical symmetry, dragging the lateral structures that come close to each other, thus pulling the long arms and compressing the short ones. From this correlation, it is also possible to determine that the load is almost likewise distributed between the arms, being the local strain the same under an equal global load. This is very useful data to measure, as it can be used as a design requirement for the actual NiTi auxetic geometry. In fact, in the structure made of NiTi, the level of deformation of the individual parts is correlated to their degree of transformation, and therefore a homogenous deformation value guarantees that the whole NiTi cell works collaboratively. Furthermore, the local measurements allowed us to verify that the hysteresis observed on the global behavior of the ABS + structure, Fig. 4(a), is correlated with the complex geometry since the relation between load and local strain is perfectly linear, Fig. 4(c). This outcome has an interesting implication for the design of the NiTi structure since the ABS cell only expresses the hysteresis share due to the geometry, removing the effect due to the pseudoelastic material. Local measurements of the strain and/or stress state could therefore help in discriminating, in the NiTi cell, a contribution of the auxetic geometry on the global hysteresis, although the latter is dominated by the pseudoelastic cycle of the material.

Finally, after the 1 Hz compression test, it was observed that the fracture zones are all located on the short arms, Fig. 10(b). This is due to the high deformation to which these zones are subjected during compression as result of the local strain analyses reported in Fig. 4.

5 Conclusions

The present work presents the damping response of an auxetic NiTi pseudoelastic structure fabricated through additive manufacturing. Electropolishing effects were also investigated.

It was observed that electropolishing is useful in removing the outermost layers of the specimen in order to homogenize the thermal response of NiTi parts. Moreover, short electropolishing (up to 10 min) is beneficial in terms of dissipated energy; however, electropolishing seems to have no effect on the loss factor value.

The outcomes are promising and highlight how auxetic NiTi dampers can be considered in those applications where superior mechanical outcomes associated with light weighting and functional responses are required. The proposed NiTi complex structure shows a good damping response. However, further studies should be considered in order to take into account the complex distribution of stress (and strain) within the auxetic arms. Therefore, future research should be primarily directed toward the improvement of the study of the local strains, taking advantage of the numerical modeling approach. This would help in the improvement of the final auxetic geometry.

Author contribution All authors contributed to the study's conception and design. Material preparation, data collection, and analysis were performed by Paolo Bettini, Adelaide Nespoli, Antonio Mattia Grande, and Daniela Rigamonti. The first draft of the manuscript was written by Adelaide Nespoli and Paolo Bettini, and all authors commented on previous versions of the manuscript. All authors read and approved the final manuscript.

Declarations

References

1. Otsuka K, Wayman CM (1999) Shape memory materials. Cambridge University Press, Cambridge
2. Duerig TW, Melton KN, Stöckel D, Wayman CM (1990) Engineering aspects of shape memory alloys. Butterworth-Heinemann, London. https://doi.org/10.1016/C2013-0-04566-5
3. Hartl DJ, Lagoudas DC (2007) Aerospace applications of shape memory alloys. J Aerosp Eng 221:535–552. https://doi.org/10.1243/09544100JAERO211
4. Otsuka K, Ren X (2005) Physical metallurgy of Ti–Ni-based shape memory alloys. Proc Mater Sci 50:511–678. https://doi.org/10.1016/j.pmatsci.2004.10.001
5. Frenzel J, George EP, Dlouhy A, Somsen CH, Wagner MFX, Eggeler G (2010) Influence of Ni on martensitic phase transformations in NiTi shape memory alloys. Acta Mater 58:3444–3458. https://doi.org/10.1016/j.actamat.2010.02.019
6. Nespoli A, Villa E, Bergo L, Rizzacasa A, Passaretti F (2015) DSC and three-point bending test for the study of the thermomechanical history of NiTi and NiTi-based orthodontic archwires. J Therm Anal Calorim 120:1129–1138. https://doi.org/10.1007/s10973-015-4441-3
7. Ma Y, Scarpa F, Zhang D, Zhu B, Chen L, Hong J (2013) A nonlinear auxetic structural vibration damper with metal rubber particles. Smart Mater Struct 22:084012. https://doi.org/10.1088/0964-1726/22/8/084012
8. Zhang J, Lu G, You Z (2020) Large deformation and energy absorption of additively manufactured auxetic materials and structures: a review. Composites Part B 2020:108340. https://doi.org/10.1016/j.compositesb.2020.108340
9. Al-Rifaie H, Sumelka W (2019) The development of a new shock absorbing uniaxial graded auxetic damper (UGAD). Materials 12:2573. https://doi.org/10.3390/ma12162573
10. Zhang W, Ma Z, Hu P (2014) Mechanical properties of a cellular vehicle body structure with negative Poisson's ratio and enhanced strength. J Reinf Plast Comp 33(4):342–349. https://doi.org/10.1177/0731684413510752
11. Sun J, Guan Q, Liu Y, Leng J (2016) Morphing aircraft based on smart materials and structures: a state-of-the-art review. J Intel Mater Sys Struct. https://doi.org/10.1177/1045389X16629569
12. Prall D, Lakes RS (1997) Properties of a chiral honeycomb with a Poisson's ratio of -1. Int J Mech Sci. https://doi.org/10.1016/S0020-7403(96)00025-2
13. Santulli C, Langella C (2016) Study and development of concepts of auxetic structures in bio-inspired design. Int J Sust Des. https://doi.org/10.1504/IJSDES.2016.078947
14. Günaydın K, Eren Z, Kazancı Z, Scarpa F, Grande AM, Süleyman Türkmen H (2019) In-plane compression behavior of anti-tetrachiral and re-entrant lattices. Smart Mater Struct. https://doi.org/10.1088/1361-665X/ab47c9
15. Airoldi A, Rigamonti D, Sala G, Bettini P, Villa E, Nespoli A (2021) Development of an actuated corrugated laminate for morphing structures. Aeron J 125:180–204. https://doi.org/10.1017/aer.2020.70
16. Ashby MF, Gibson LJ (1997) Cellular solids: structure and properties. Press Syndicate of the University of Cambridge, Cambridge, UK
17. Prawoto Y (2012) Seeing auxetic materials from the mechanics point of view: a structural review on the negative Poisson's ratio. Comp Mater Sci 58:140–153. https://doi.org/10.1016/j.commatsci.2012.02.012
18. Yang H, Sakai K, Shizuka H, Kurebayashi Y, Hayakawa K, Nagare T (2021) Experimental investigation of the effects of superelasticity on the machinability of NiTi alloys. Int J Adv Manuf Tech 115:581–593. https://doi.org/10.1007/s00170-021-07166-4
19. Petrini L, Migliavacca F (2011) Biomedical applications of shape memory alloys. J Metall. https://doi.org/10.1155/2011/501483
20. Wen C, Yu X, Zeng W, Zhao S, Wang L, Wan G, Huang S, Grover H, Chen Z (2018) Mechanical behaviors and biomedical applications of shape memory materials: a review. AIMS MaterSci 5:559–560. https://doi.org/10.3934/matersci.2018.4.559
21. Nespoli A, Dallolio V, Villa E, Passaretti F (2015) A new design of a Nitinol ring-like wire for suturing in deep surgical field. Mater Sci Eng C 56:30–36. https://doi.org/10.1016/j.msec.2015.06.009
22. Barbarino S, Saavedra Flores EI, Ajaj RM, Dayyani I, Friswell MI (2014) A review on shape memory alloys with applications to morphing aircraft. Smart Mater Struct. https://doi.org/10.1088/0964-1726/23/6/063001
23. McDonald Schetky L (1991) Shape memory alloy applications in space systems. Mater Des 12:29–32. https://doi.org/10.1016/0261-3069(91)90089-M
24. Dutta SC, Majumder R (2019) Shape memory alloy (SMA) as a potential damper in structural vibration control. in Proc. 2019 of the Inter. Conf. on Manufacturing Engineering and Materials (Eds: S. Hloch, D. Klichová, G. Krolczyk, S. Chattopadhyaya, L. Ruppenthalová), Springer, Cham
25. Borlandelli E, Scarselli D, Nespoli A, Rigamonti D, Bettini P, Morandini M, Villa E, Sala G, Quadrio M (2015) Design and experimental characterization of a NiTi-based, high-frequency, centripetal peristaltic actuator. Smart Mater Struct. https://doi.org/10.1088/0964-1726/24/3/035008
26. Nespoli A, Rigamonti D, Riva M, Villa E, Passaretti F (2016) Study of pseudoelastic systems for the design of complex passive dampers: static analysis and modeling. Smart Mater Struct. https://doi.org/10.1088/0964-1726/25/10/105001
27. Chen QF, Zuo XB, Wang LM, Chang W, Tian WY, Li AQ, Yang H, Liu LH (2006) NiTi wire as a superelastic damping material in structural engineering. Mater Sci Eng A 438–440:1089–1092. https://doi.org/10.1016/j.msea.2006.02.196
28. Nespoli A, Bassani E, Della Torre D, Donnini R, Villa E, Passaretti F (2017) An experimental study on pseudoelasticity of

a NiTi-based damper for civil applications. Smart Mater Struct. https://doi.org/10.1088/1361-665X/aa882e

29. DebRoy T, Wei HL, Zuback JS, Mukherjee T, Elmer JW, Milewski JO, Beese AM, Wilson-Heid A, Ded A, Zhang W (2018) Additive manufacturing of metallic components – process, structure and properties. Prog Mater Sci 92:112–224. https://doi.org/10.1016/j.pmatsci.2017.10.001

30. Herzog D, Seyda V, Wycisk E, Emmelmann C (2016) Additive manufacturing of metals. Acta Mater 117:371–392

31. Song B, Zhao X, Li S, Han C, Wei Q, Wen S, Liu J, Shi Y (2015) Differences in microstructure and properties between selective laser melting and traditional manufacturing for fabrication of metal parts: a review. Frontiers Mech Eng 10:111–125. https://doi.org/10.1007/s11465-015-0341-2

32. Gokuldoss PK, Kolla S, Eckert J (2017) Additive manufacturing processes: selective laser melting, electron beam melting and binder jetting—selection guidelines. Mater. https://doi.org/10.3390/ma10060672

33. Yap CY, Chua CK, Dong ZL, Liu ZH, Zhang DQ, Loh LE, Sing SL (2015) Review of selective laser melting: materials and applications. App Phys Rev DOI 10(1063/1):4935926

34. Yadroitsev I, Smurov I (2010) Selective laser melting technology: from the single laser melted track stability to 3Dparts of complex shape. Phys Proc 5:551–560. https://doi.org/10.1016/j.phpro.2010.08.083

35. Nespoli A, Grande AM, Bennato N, Rigamonti D, Bettini P, Villa E, Sala G, Passaretti F (2021) Towards an understanding of the functional properties of NiTi produced by powder bed fusion. Prog Add Man 6:321–337. https://doi.org/10.1007/s40964-020-00155-1

36. Rakshith B, Sreesha RB, Ladakhan SH, Mudakavi D, Adinarayanappa SM (2022) An experimental investigation on performance of NiTi-based shape memory alloy 4D printed actuators for bending application. Int J Adv Manuf Tech 122:4421–4436. https://doi.org/10.1007/s00170-022-09875-w

37. Farjam N, Nematollahi M, Andani MY, Mahtabi MJ, Elahinia M (2020) Effects of size and geometry on the thermomechanical properties of additively manufactured NiTi shape memory alloy. Int J Adv Manuf Tech 107:3145–3154. https://doi.org/10.1007/s00170-020-05071-w

38. Lv J, Shen H, Fu J (2022) Fabrication of multi-functional Ni–Ti alloys by laser powder bed fusion. Int J Adv Manuf Tech 119:357–365. https://doi.org/10.1007/s00170-021-08039-6

39. Xiong Z, Li Z, Sun Z, Hao S, Yang Y, Li M, Song C, Qiu P, Cui L (2019) Selective laser melting of NiTi alloy with superior tensile property and shape memory effect. J Mater Sci & Tech 35:2238–2242. https://doi.org/10.1016/j.jmst.2019.05.015

40. Li S, Hassanin H, Attallah MM, Adkins NJE, Essa K (2016) The development of TiNi-based negative Poisson's ratio structure using selective laser melting. Acta Mater 105:75–83. https://doi.org/10.1016/j.actamat.2015.12.017

41. Saghaian SE, Amerinatanzi A, Moghaddam NS, Majumdar A, Nematollahi M, Saedi S, Elahinia M, Karaca HE (2018) Mechanical and shape memory properties of triply periodic minimal surface (tpms) NiTi structures fabricated by selective laser melting. Biol Eng Med 2. https://doi.org/10.15761/BEM.1000152

42. Saedi S, Saghaian SE, Jahadakbar A, Moghaddam NS, Andani MT, Saghaian SM, Lu YC, Elahinia M, Karaca HE (2018) Shape memory response of porous NiTi shape memory alloys fabricated by selective laser melting. J Materi Sci Mater Med. https://doi.org/10.1007/s10856-018-6044-6

43. Karamooz Ravari MR, Nasr Esfahani S, Taheri Andani M, Kadkhodaei M, Ghaei A, Karaca H, Elahinia M (2016) On the effects of geometry, defects, and material asymmetry on the mechanical response of shape memory alloy cellular lattice structures. Smart Mater Struct. https://doi.org/10.1088/0964-1726/25/2/025008

44. Nespoli A, Bettini P, Villa E, Sala G, Passaretti F, Grande M (2021) A study on damping property of NiTi elements produced by selective laser-beam melting. Adv Eng Mater. https://doi.org/10.1002/adem.202001246

45. Ferchow J, Hofmann U, Meboldt M (2020) Enabling electropolishing of complex selective laser melting structure. Procedia CIRP 91:472–477

46. Nespoli A, Passaretti F, Villa E (2013) Phase transition and mechanical damping properties: a DMTA study of NiTiCu shape memory alloys. Intermetal 32:394–400. https://doi.org/10.1016/j.intermet.2012.09.005